



Ballistic performance of ultralight multifunctional cellular sandwich plates with UHMWPE fiber metal laminate skins

Rui Zhang^{a,b,c}, Bin Han^{c,*}, Yi Zhou^a, Lu-Sheng Qiang^{b,d}, Qi Zhang^c, Qian-Cheng Zhang^e, Tian Jian Lu^{b,d,*}

^a State Key Laboratory of New Textile Materials and Advanced Processing Technologies, Wuhan Textile University, Wuhan 430200, P.R. China

^b State Key Laboratory of Mechanics and Control of Mechanical Structures, Nanjing University of Aeronautics and Astronautics, Nanjing 210016, P.R. China

^c School of Mechanical Engineering, Xi'an Jiaotong University, Xi'an 710049, P.R. China

^d MIIT Key Laboratory of Multifunctional Lightweight Materials and Structures, Nanjing University of Aeronautics and Astronautics, Nanjing 210016, P.R. China

^e School of Aerospace Engineering, Xi'an Jiaotong University, Xi'an 710049, P.R. China

ARTICLE INFO

Keywords:

Sandwich plate
Fiber metal laminates
Penetration
Blast
Bending
Multifunctionality

ABSTRACT

While an ultralight sandwich construction with cellular core can be tailored to exhibit superior load-bearing capability and blast resistance, its ballistic performance is typically inferior to its equivalent monolithic counterpart. To improve the projectile penetration resistance while maintaining the capability of load bearing and blast mitigation, this work proposed a multifunctional sandwich plate with ultra-high molecular weight polyethylene (UHMWPE) fiber metal laminate (FML) skins and aluminum honeycomb core. A combined experimental and numerical approach was employed to quantify the ballistic performance, assess the penetration process, and reveal the underlying mechanisms of the novel sandwich construction. In addition to ballistic resistance, its performance under three-point bending as well as impulsive shock loading was also assessed for multifunctional applications. Relative to all-metallic honeycomb sandwich plate having identical areal density, incorporating UHMWPE composite layers into the skin improved significantly the penetration resistance: the failure mode of the laminate skin was changed from local shear-plugging to global dishing and cracking, enabling enhanced energy absorption of the thin metallic (titanium) layers. Moreover, the use of UHMWPE FML skin for sandwich construction led to not only significantly enhanced bending capacity but also reduced maximum deflection under impulsive shock loading. Hence, the proposed cellular sandwich plate with UHMWPE FML skins can be designed as ultralight multifunctional structure with simultaneous load-bearing and blast/ballistic resistant capabilities.

1. Introduction

All-metallic sandwich constructions with two thin skins (also known as face sheets or, simply, faces) and cellular truss cores are ultralight primary structures that exhibit not only high specific stiffness/strength [1–6] but also superior energy absorption under impact and blast loadings [7–9], thus enabling a multitude of engineering applications. In addition to bearing structural load and absorbing impact energy, a cellular sandwich plate with fluid-through topology can also serve as a heat exchanger for active cooling [10–12] or a sound absorber when micro-perforations (submillimeter scale) are introduced to its skin facing the incident sound [13,14]. Nonetheless, although it has been established that all-metallic cellular sandwich constructions possess attractive multifunctional attributes, their performance under ballistic

impacts is no better than monolithic metallic plates of equal mass [15,16]. In aerospace applications, ultralight sandwich structures commonly found in modern aircraft and space vehicles are susceptible to high velocity impact by a variety of objects (projectiles), such as orbital debris, birds, hailstones, and fragment clusters, which may severely damage the structure [17]. All-metallic corrugated sandwiches are also increasingly exploited for marine construction (e.g., ship hulls) due to high structural efficiency and outstanding mitigation on impact loading caused by, say, explosion by anti-ship missiles. With great kinetic energy, these missiles are able to pierce the hull of a naval vessel with severe perforation, while the fragmentation of warhead casing and damaged hull structures during explosion generates high-velocity fragment clusters. Therefore, how to design ultralight, structural load-bearing cellular sandwiches against simultaneous blast and ballistic

* Corresponding authors.

E-mail addresses: hanbinghost@mail.xjtu.edu.cn (B. Han), tjlu@nuaa.edu.cn (T.J. Lu).

<https://doi.org/10.1016/j.compstruct.2022.116390>

Received 5 April 2022; Received in revised form 12 September 2022; Accepted 14 October 2022

Available online 20 October 2022

0263-8223/© 2022 Elsevier Ltd. All rights reserved.

loading remains a critical challenge to be addressed.

The disappointing ballistic performance of ultralight all-metallic sandwich structures with cellular truss cores is expected, and can be attributed to two main reasons. First, projectile penetration in such a sandwich structure causes plug formation in its skins and stretching/bending or fracture of its core, both being less effective at impeding projectile penetration than an equivalent monolithic plate that resists penetration mostly by adiabatic shearing. Second, while the skins (albeit thin) of the sandwich play a major role in resisting projectile penetration and energy absorption, the core only plays a minor role [18,19]. In recent years, to enhance the ballistic resistance of cellular sandwich structures, the concept of hybrid core construction was proposed. For instance, filling the cellular core (e.g., triangular corrugations and square honeycombs) of an all-metallic sandwich structure with ceramic [20,21] or concrete [22] prisms as well as polymers [23] led to significantly enhanced ballistic performance. Nevertheless, the proposed hybrid core with material filling not only increases the weight but also alters the porous feature of sandwich core important for other attributes such as energy absorption and active cooling, thus restricting further applications of sandwich constructions with hybrid cores.

Alternatively, replacing the traditionally monolithic skins of a sandwich structure with hybrid skins, e.g., fiber metal laminates (FMLs), has become a fascinating option to elevate its ballistic resistance, especially for applications in weight sensitive fields such as aerospace engineering. Over the past decades, the FMLs, consisting of alternating metal layers and fiber-reinforced-plastic layers, have drawn tremendous interests for unique advantages in low-velocity impact, fatigue resistance, and fracture toughness [24]. For typical instance, numerous experimental studies have been performed on the ARALLs (aramid fiber reinforced aluminum laminates) [25], GLAREs (glass fiber reinforced aluminum laminates) [26,27], and CARALLs (carbon fiber reinforced aluminum laminates) [28]. In general, the initial failures of the ARALLs and CARALLs are dominated by fibers, whereas the critical failure mechanism of the GLAREs is controlled by aluminum layer. Accordingly, due to difference in failure modes, the GLAREs exhibit the highest impact resistance as the ARALL and CARALLs can be penetrated more easily [29].

At present, although the GLAREs have been exploited as the skins of sandwich structures [30,31], only slight enhancement was achieved in energy absorption efficiency under high velocity projectile impact [32]. This was because the deformation area of a GLARE skin was mostly confined to a relatively small area surrounding the impact site [27], rather than absorbing projectile energy through the more efficient global deformation. Hence, significant improvement in ballistic resistance has not been achieved. Moreover, existing studies mainly focused on sandwiches having glass FML skins and cellular foam cores, and little attention was paid on sandwich constructions with alternative FML skin types and lattice truss cores. Further, detailed damage modes and failure mechanisms under ballistic impact were rarely reported.

There has been considerable interest in using ultra-high molecular weight polyethylene (UHMWPE) fiber composite to construct light-weight protective structures targeting ballistic impacts, due to its low density (less than that of water) and high specific strength [33,34]. Abundant experimental and numerical investigations have shown that, when subjected to high velocity projectile impact, a UHMWPE laminate typically fails progressively towards eventual large out-of-lane deflection, thus enabling great energy absorption [35]. For example, under the impact of either 12.7 mm or 20 mm fragment simulating projectile, UHMWPE composite laminates were found to be consistently more mass efficient than polymer composite laminates reinforced by aramid, glass and carbon fibers [34]. It had also been demonstrated that the UHMWPE composite has the capability to enhance the ballistic performance of ceramic/metal bi-layer armors without adding significant weight [36]. In particular, it was experimentally found that the ballistic limit of UHMWPE FML was about 30 % higher than that of carbon FML having equal areal density [37]. Consequently, it is envisioned that ultralight

cellular sandwich constructions with UHMWPE FML skins are promising for multifunctional applications requiring simultaneous ultralight-weight, superior load-bearing capability, outstanding impact energy absorption, and high ballistic resistance. As previously mentioned, additional attributes can also be achieved with such sandwich constructions, such as sound absorption and active cooling.

The current study proposed a novel honeycomb sandwich structure with UHMWPE FML skins, and the effectiveness of using such novel skins to enhance the penetration resistance of the sandwich was systematically explored. Each UHMWPE FML skin was consisted of thin titanium alloy (Ti-6Al-4V) layers and UHMWPE composite layers. A combined experimental and numerical approach was employed to quantify the ballistic performance of the proposed sandwich construction, assess the penetration process, and reveal the underlying physical mechanisms. How the configurations and bonding conditions of the UHMWPE FML skins affect the ballistic response was also discussed. In addition, for multifunctional applications requiring simultaneous load-bearing and blast/ballistic resistant capabilities, the performance of the proposed sandwich under quasi-static three-point bending and shock loading was characterized and compared with its all-metallic counterpart having equal areal density.

2. Experimental investigations

2.1. Materials and specimens

The UHMWPE FML skins proposed in the current study were manufactured with thin titanium alloy (Ti-6Al-4V) layers and thin UHMWPE composite layers. Targeting aerospace applications, the titanium alloy was selected for low density and high specific strength. The UHMWPE composite pre-pregs (HA792, acquired from Beijing Tongyizhong New Material Technology Co.) were comprised of two orthogonal unidirectional plies, and each pre-preg had a thickness of 0.15 mm. The fibers had a tensile strength of 3.8 GPa and were bonded by polyurethane resin, resulting in a fiber volume fraction of 83 %. A total of eight pre-pregs were hot-pressed at 127 °C under a pressure of 20 MPa, forming a UHMWPE composite layer with a thickness of 1 mm and an areal density of 0.96 kg/m². Each titanium layer had a thickness of 0.5 mm and an areal density of 2.23 kg/m². Epoxy adhesive (Loctite Hysol E-120HP) was used to bond the UHMWPE composite layer to the titanium layer. Before bonding, the surfaces of each titanium layer were cleaned by ultrasonic and ethanol. Subsequently, upon mixing the epoxy resin and curing agent at a volume ratio of 2:1, the mixture was evenly applied on each titanium layer. A hand lay-up process was adopted by alternately stacking the titanium and UHMWPE layers. The resulting FML assembly was cured at room temperature under a pressure of 6 kPa for 24 h.

Aluminum hexagonal honeycombs made of 3003-H18 (acquired from Beijing Honeyfei New Materials Co.) were chosen as the sandwich core and bonded to the UHMWPE FML or titanium skins by epoxy adhesive; Fig. 1(a). As illustrated in Fig. 1(b), each hexagonal cell (side length $L_c = 2$ mm) was consisted of four single-thickness walls ($T_c = 0.05$ mm) and two double-thickness walls. For the present sandwich construction, the height and area density of honeycomb core were fixed at $H_c = 20$ mm and 2.7 kg/m², respectively.

Three different types of square sandwich specimen, with side length fixed at $L = 300$ mm, were fabricated for ballistic testing, as shown in Fig. 1(c) and Table 1. The sandwich specimens had the same honeycomb core but different skins. Specimen type 'MF' implied that 2 mm monolithic titanium plates were used as skins, Specimen type 'FML-S' indicated that its FML skins consisted of a single UHMWPE composite layer and two titanium layers, while Specimen type 'FML-D' indicated its FML skins had two UHMWPE composite layers and three titanium layers. For the 'MF' and 'FML-S' specimens, the same sandwich thickness was maintained and hence the latter was about 34 % lighter in weight. In contrast, the 'MF' and 'FML-D' specimens had similar areal densities to

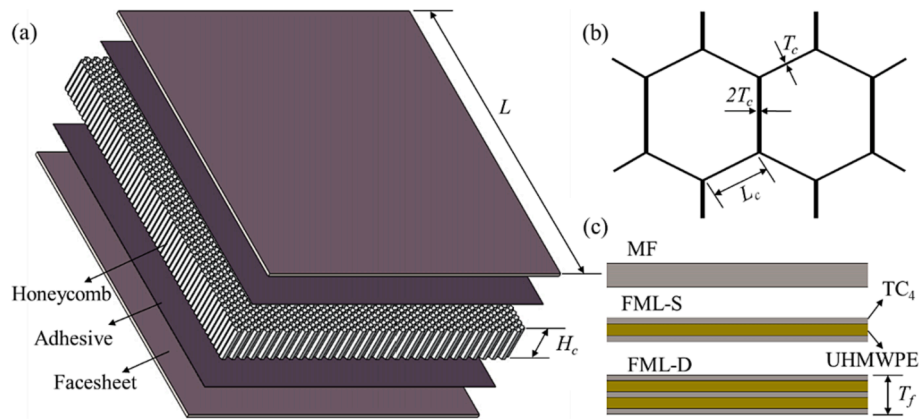


Fig. 1. Schematic of (a) honeycomb sandwich panel with UHMWPE FML skins, (b) hexagonal honeycomb, and (c) monolithic titanium skin and FML skins.

Table 1
Configurations of sandwich specimens.

| Specimen type | Skin | | Honeycomb core | | | Areal density (kg/m ²) |
|---------------|----------------|-----------------|----------------|------------|------------|------------------------------------|
| | Configuration | T_f (mm) | H_c (mm) | L_c (mm) | T_c (mm) | |
| MF | Ti | 2 | 20 | 2 | 0.05 | 20.50 |
| FML-S | Ti/PE/Ti | 0.5/1/0.5 | | | | 13.52 |
| FML-D | Ti/PE/Ti/PE/Ti | 0.5/1/0.5/1/0.5 | | | | 19.89 |

allow for direct comparison of ballistic performance. Note that, for the skins of both 'FML-S' and 'FML-D' specimens, each UHMWPE composite layer is sandwiched between two titanium layers such that the latter is directly bonded to the honeycomb core, not the former.

2.2. Protocol for ballistic impact tests

With reference to Fig. 2, ballistic impact tests of as-fabricated sandwich specimens were conducted using a nitrogen gas gun. During the tests, the projectile was accelerated by the gas gun to impact at the center of each specimen at normal incidence. Cylindrical blunt projectiles made of AISI4340 steel were selected, each having a diameter of 7.62 mm, a length of 20 mm and a mass of 7.1 g. Since the diameter of the gas gun barrel was 10 mm, a sabot made of polyethylene was designed to carry the projectile. During the impact tests, it was observed that the sabot was attached behind the projectile, as discussed later in Section 4.1. Due to the low density and strength of the sabot material,

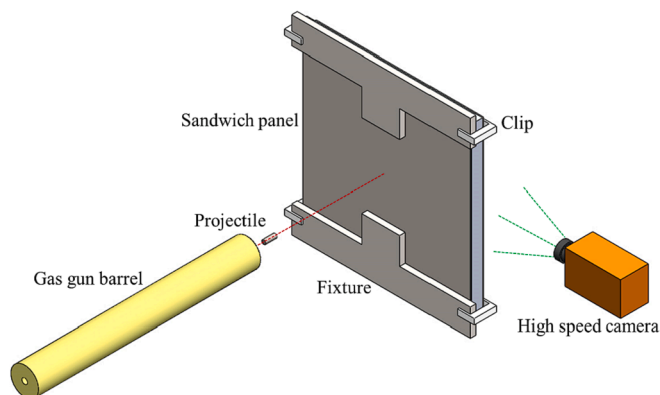


Fig. 2. Experimental setup of ballistic impact test and clamp condition of sandwich specimen.

the influence of sabot on ballistic response was neglected in the present study. The gas pressure in a chamber was used to control the projectile velocity, which ranged from 350 m/s to 650 m/s. Four clips were used to clamp each sandwich specimen to the fixture. A high-speed camera (IX I-SPEED 510) was used to capture the impact and residual velocities of each projectile and record its dynamic penetration process across the sandwich specimen. The exposure time and frame rate were set to be 2 μ s and 100,000 FPS, respectively. Thus, the time interval between two sequentially captured pictures was 10 μ s.

3. Numerical simulations

3.1. Finite element model

Three-dimensional finite element (FE) models were established with the commercial software LS-DYNA, as shown schematically in Fig. 3(a). In general, the honeycomb could be modeled by an equivalent homogeneous core, and the corresponding effective material properties could be obtained from either theoretical or computational methods [38,39]. However, in high-velocity impact events, the damage of honeycomb would be concentrated around the impact location, and the local crushing was much more serious than the global deformation. Therefore, the real geometry of honeycomb core was employed in FE simulations to capture the ballistic response with sufficient accuracy.

Since the sandwich specimens for impact tests were large enough with respect to the selected projectile, and the experimentally observed deformation region of each specimen was much smaller than the length of the sandwich. Further, as the relatively weak constraint was applied to sandwich specimens in the impact experiments (as shown in Fig. 2), the edge condition was approximated as free boundary, i.e., no boundary conditions were imposed on sandwich plates in the FE models. It has been well established that the free boundary was suitable for simulating the penetration process of large target plates [22,35]. As the initial loading condition, the initial velocity of each projectile was defined.

The skins of each sandwich and the projectile were all meshed by the reduced integration solid elements (SOLID 164), while the honeycomb core was modelled using shell elements (SHELL 163) with Belytschko-Wong-Chiang formulation [40]. For 'MF' specimen, a mesh refinement study was performed and demonstrated that the predicted residual velocity increased with the decrease of element size. The numerical convergence could be reached for cases with the element size smaller than 0.67 mm. Therefore, a global mesh size of 0.5 mm was employed for the projectile and the honeycomb core. For titanium skins, a biased mesh was adopted, with mesh details of 'MF' specimen displayed in Fig. 3(b). Each titanium layer was divided into three elements in the thickness direction, with an in-plane length of 0.67 mm. For each UHMWPE composite layer with the thickness of 1 mm, two elements were meshed in the thickness direction, with an in-plane mesh size of

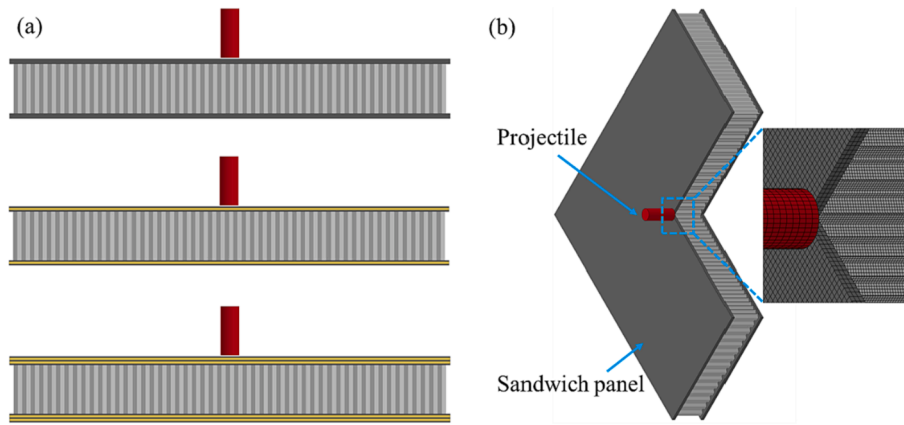


Fig. 3. (a) Finite element models for ‘MF’, ‘FML-S’ and ‘FML-D’ sandwich specimens and (b) mesh details of ‘MF’ specimen.

0.5 mm. The total number of elements in the ‘MF’ model was 2488550, while those in the ‘FML-S’ and ‘FML-D’ models were 2,553,350 and 2747750, respectively. According to the mesh sensitivity analysis, the above meshing sizes were sufficient for numerical convergence, and further mesh refinement had little improvement on the accuracy but greater sacrifice of computational time.

Surface-to-surface tiebreak contacts were adopted to simulate the bond between adjacent UHMWPE composite and titanium layers. According to the properties of cured epoxy adhesive, a normal failure strength I_n of 41 MPa and a shear failure strength I_s of 30 MPa were defined [41]. The failure criterion of adhesive bonding was thence given by:

$$\left(\frac{\sigma_n}{I_n}\right)^2 + \left(\frac{\sigma_s}{I_s}\right)^2 \geq 1 \quad (1)$$

where σ_n and σ_s were the normal and shear stresses at the bond. When the failure criterion was met, delamination/debonding occurred. Further, nodes-to-surface tiebreak contacts were used to simulate adhesive bonding between the skins and the honeycomb core, with the same cohesive strengths adopted. Eroding contact options were applied between the projectile and sandwich components. An hourglass control methodology was employed to counter the non-physical modes of deformation.

3.2. Material constitutive models

Mechanical responses of the metallic materials used in current experiments – titanium for the skins, steel for the projectiles, and aluminum for the honeycomb core – were simulated with the well-established Johnson-Cook (JC) constitutive law, which was applicable to large deformation, with effects of strain rate, strain hardening, and thermal softening accounted for. According to the JC constitutive law, the flow stress σ_y was expressed as [42]:

$$\sigma_y = (A + B\bar{\epsilon}^p)(1 + c \ln \dot{\epsilon}^*) (1 - T^{*m}) \quad (2)$$

where A , B , c , n and m were material constants, $\bar{\epsilon}^p$ was the effective plastic strain, $\dot{\epsilon}^*$ was the effective plastic strain rate, and T^* was the dimensionless temperature. In addition, the strain at fracture ϵ^f was given by [42]:

$$\epsilon^f = (d_1 + d_2 \exp(d_3 \sigma^*)) (1 + d_4 \ln \dot{\epsilon}^*) (1 + d_5 T^*) \quad (3)$$

where d_1 , d_2 , d_3 , d_4 and d_5 were material constants, and σ^* was the stress triaxiality. Table 2 listed relevant material parameters for steel AISI4340, titanium Ti-6Al-4 V, and aluminum 3003-H18, all taken from existing studies [19,42,43].

The UHMWPE cross-ply composite was simulated using a composite

Table 2

Material constants for steel AISI 4340 [42], titanium Ti-6Al-4 V [43], and aluminum 3003-H18 [19].

| Material Constants | AISI 4340 | Ti-6Al-4 V | 3003-H18 |
|--|-----------|------------|----------|
| Density, ρ (g/cm ³) | 7.8 | 4.45 | 2.68 |
| Shear modulus, G (GPa) | 77.0 | 41.9 | 25.4 |
| Static yield strength, A (GPa) | 0.95 | 0.86 | 0.214 |
| Strain hardening constant, B (GPa) | 0.51 | 0.331 | 0.143 |
| Strain hardening exponent, n | 0.26 | 0.34 | 0.36 |
| Strain rate constant, c | 0.014 | 0.012 | 0.015 |
| Thermal softening exponent, m | 1.03 | 0.6 | 1.7 |
| Reference strain rate, $\dot{\epsilon}_0$ (s ⁻¹) | 1.0 | 1.0 | 1.0 |
| Melting temperature, t_m (K) | 1793 | 1875 | 893 |
| Specific heat, C , (J/kg K) | 477 | 560 | 875 |
| Damage constant, d_1 | 0.05 | -0.09 | 1.0 |
| Damage constant, d_2 | 3.44 | 0.27 | 0 |
| Damage constant, d_3 | -2.12 | 0.48 | 0 |
| Damage constant, d_4 | 0.002 | 0.014 | 0 |
| Damage constant, d_5 | 0.61 | 3.87 | 0 |

damage model for solid elements, i.e., the material type #59 within LS-DYNA: the composite was taken as orthotropic elastic, with equal properties along both fiber directions denoted separately by subscripts ‘x’ and ‘y’. Three failure modes were activated, with corresponding criteria summarized in Table 3, while the elastic stiffness and strength parameters taken from references [35,44] were listed in Table 4. Values of the three shear strengths (S_{xy} , S_{xz} , S_{yz}) were set to infinite due to the large shear strain at failure typically measured for UHMWPE composites [45]. Accordingly, in-plane tensile failure and through-thickness compressive failure modes were mainly dominated by the corresponding tensile strengths (T_{xx} , T_{yy}) and compressive strength (C_{zz}). Once a failure mode was triggered, the corresponding stiffness would be degraded. The degradation occurred only in the corresponding direction without affecting the other stress criteria computation, which was quantified by introducing scaling factors. It took 100 time-steps for the corresponding scaling factors to change from a starting value of 1.0 to a

Table 3

Failure criteria of UHMWPE cross-ply composite.

| Failure mode | Criterion |
|---------------------------------------|---|
| In-plane tensile failure | $\left(\frac{\sigma_{xx}}{T_{xx}}\right)^2 + \left(\frac{\tau_{xy}}{S_{xy}}\right)^2 + \left(\frac{\tau_{xz}}{S_{xz}}\right)^2 \geq 1$ (1) |
| | $\left(\frac{\sigma_{yy}}{T_{yy}}\right)^2 + \left(\frac{\tau_{xy}}{S_{xy}}\right)^2 + \left(\frac{\tau_{yz}}{S_{yz}}\right)^2 \geq 1$ (2) |
| Through-thickness compressive failure | $\left(\frac{\sigma_{zz}}{S_{xz} + S_{yz}}\right)^2 + \left[\left(\frac{C_{zz}}{S_{xz} + S_{yz}}\right)^2 - 1\right] \frac{\sigma_{zz}}{ C_{zz} } + \left(\frac{\tau_{xz}}{S_{xz}}\right)^2 + \left(\frac{\tau_{yz}}{S_{yz}}\right)^2 \geq 1$ (3) |

Table 4
Material parameters for UHMWPE cross-ply composite [35,44].

| Property | Value |
|--|--------|
| Young's modulus, E_{xx}, E_{yy} (GPa) | 34.257 |
| Young's modulus, E_{zz} (GPa) | 5.1 |
| Poisson ratio, ν_{yx} | 0 |
| Poisson ratio, ν_{zx}, ν_{zy} | 0.013 |
| Shear modulus, G_{xy} (GPa) | 0.1738 |
| Shear modulus, G_{xz}, G_{yz} (GPa) | 0.5478 |
| Compressive strength, C_{zz} (GPa) | 1.74 |
| Tensile strength, T_{xx}, T_{yy} (GPa) | 1.25 |

final value of zero, thereby reducing the stress components to zero. Thus, the degradation was performed over a small computational time, corresponding to a rapid decay of the stress-strain relationship [46]. Further, element deletion was controlled by a tensile strain of 0.4 and a compressive volumetric strain of 0.8 [44].

4. Results and discussion

4.1. Experimental observations

The results obtained from the present ballistic impact tests were summarized in Table 5 and plotted in Fig. 4. Within the range of impact velocity considered, all the sandwich specimens were perforated. Since the steel projectile was sufficiently stiff relative to the skins and honeycomb core, its mass remained unchanged after impact. Energy conservation thence dictated that the energy absorbed by each specimen could be calculated based on the initial and residual kinetic energies of the projectile. Moreover, specific energy absorption (SEA) was obtained by dividing the impact energy absorbed by each specimen by areal mass density, which represented its energy absorption capacity per unit areal mass density.

From Fig. 4(a), it was found that, for similar impact velocities, the residual velocity of specimen 'FML-D' was the smallest among the three specimen types, thus implying its enhanced resistance to projectile penetration. Irrespective of specimen types, the SEA increased with increasing impact velocity, as shown in Fig. 4(b). Upon comparing the SEA values of 'MF-500' and 'FML-D-456' ('MF-500' denoted a 'MF' specimen impacted at 500 m/s while 'FML-D-456' denoted a 'FML-D' specimen impacted at 456 m/s; similar denotations applied to other specimens in subsequent analysis), a significant improvement in energy absorption (>23 % for SEA) could be observed. For impact velocities below 500 m/s, 'MF' and 'FML-S' exhibited similar SEAs, but the latter had a smaller SEA when the impact velocity reached 600 m/s. As discussed later in Section 4.3, the unexpected inferior performance of 'FML-S' was attributed to its poor ability to deform a steel projectile.

Fig. 5 presented images captured via a high-speed camera, which showed sequentially the process of projectile penetrating a 'MF' specimen at 405 m/s, a 'FML-S' specimen at 350 m/s, and a 'FML-D' specimen at 456 m/s. It could be seen that, before impact, the sabot was

Table 5
Experimental results for three different types of sandwich specimens subjected to ballistic impacts.

| Specimen type | Number | Impact velocity (m/s) | Residual velocity (m/s) | Absorbed energy (J) | Specified energy absorption ($J \cdot m^{-2}/kg$) |
|---------------|--------|-----------------------|-------------------------|---------------------|---|
| MF | 1 | 405 | 256 | 349.64 | 17.06 |
| | 2 | 500 | 368 | 406.74 | 19.84 |
| | 3 | 611 | 476 | 520.95 | 25.41 |
| FML-S | 1 | 350 | 250 | 213.00 | 15.75 |
| | 2 | 468 | 384 | 254.07 | 18.79 |
| | 3 | 622 | 544 | 322.87 | 23.88 |
| FML-D | 1 | 456 | 267 | 485.09 | 24.39 |
| | 2 | 550 | 389 | 536.69 | 26.98 |

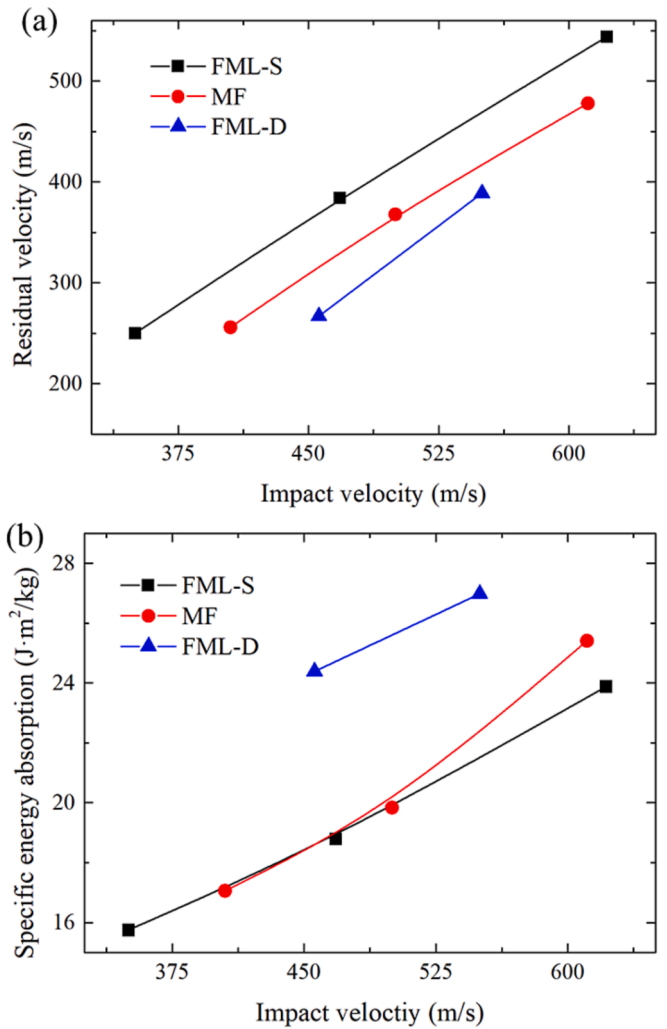


Fig. 4. Experimentally measured (a) residual velocity and (b) specific energy absorption plotted as functions of initial impact velocity for three different types of sandwich specimen.

attached behind each projectile and the two had the same velocity. As soon as impact occurred on each target plate, sparks were observed to burst from the impact location. The projectile then started to penetrate into the target, while the much weaker sabot was stopped by the front skin of the target and became fully shattered. For the three different specimen types shown in Fig. 5, the rear skin of each did not deform before 70 μs ; at around 80 μs , its out-of-plane deformation could be observed. For the 'MF' specimen, a plug was ejected in front of the projectile with sparks. For the 'FML-S' and 'FML-D' specimens, no such plug and sparks were observed: instead, bulges grew from each rear skin, thus indicating that the FML skin could attain a larger deformation under ballistic impact than its monolithic titanium counterpart. Finally, the projectile tore the bulge and left the target with fractured fibers. It should be noted that although the 'FML-D' specimen achieved a residual velocity similar to the other two specimen types, it was impacted at the highest velocity, thus its ballistic performance was superior to the other two.

Failure modes of the 'MF' specimen were displayed in Fig. 6(a). Local deformation features were observed on both the front and rear titanium skins (each 2 mm thick), and the penetration was dominated by plugging due to adiabatic shear, causing ~ 8 mm diameter circular holes. For closer examination of the honeycomb core, both titanium skins were removed from the specimen. From the front view (i.e., viewing from the direction of projectile impact), the honeycomb core deformed by

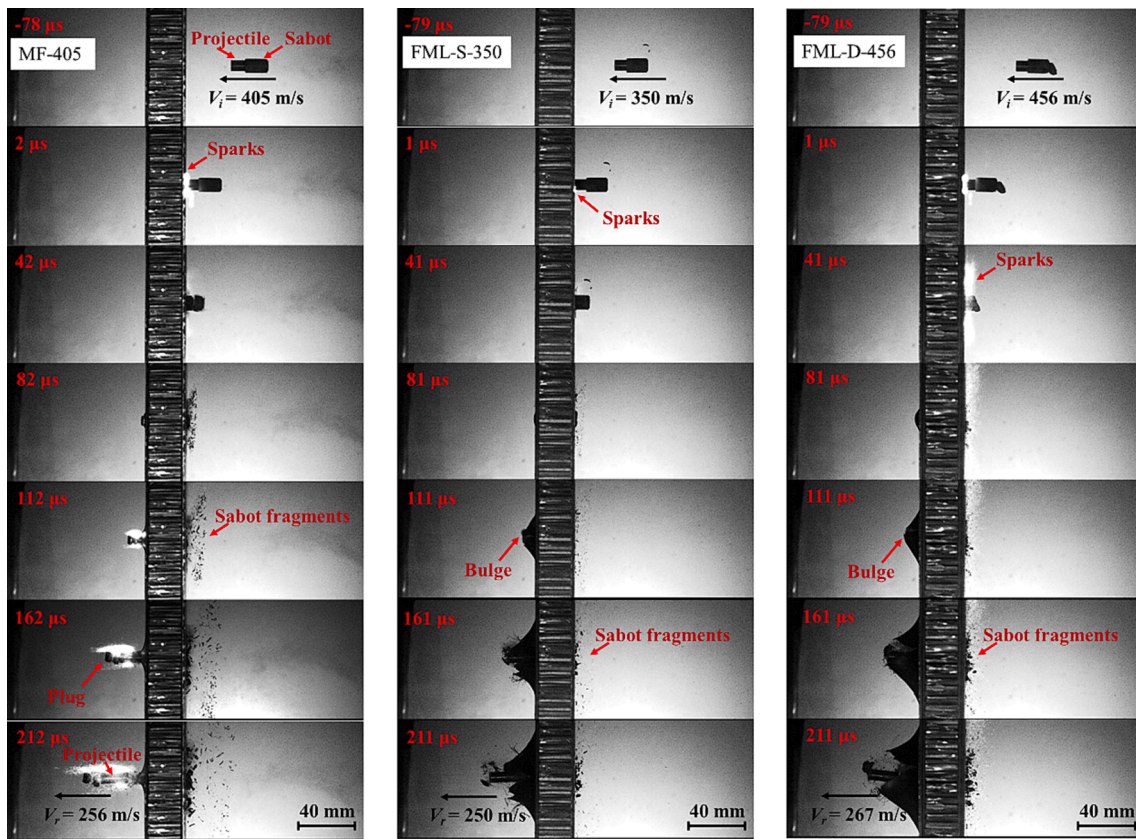


Fig. 5. High-speed camera photographs showing (from left to right) the penetration process of a ‘MF’ specimen impacted at 405 m/s, a ‘FML-S’ specimen impacted at 350 m/s, and a ‘FML-D’ specimen impacted at 456 m/s.

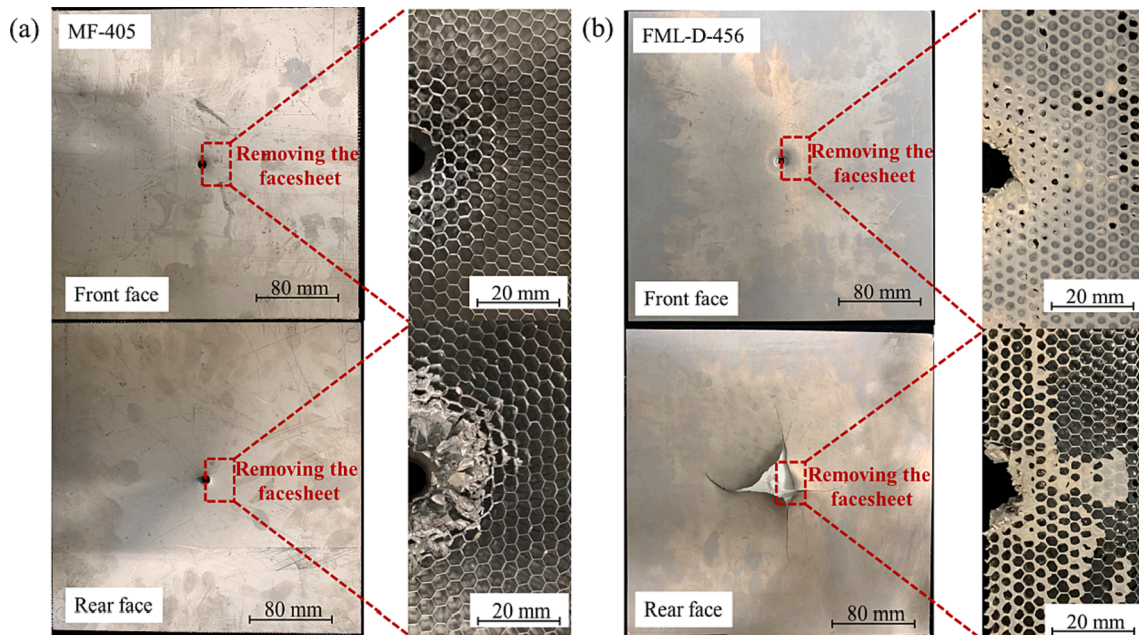


Fig. 6. Experimentally observed deformation and failure modes of (a) ‘MF’ and (b) ‘FML-D’ specimens.

buckling and folding around the impact region. From the back view, cell wall folding was not obvious but lateral compression was visible, which might be caused by splashy sparks generated by the collision between the projectile and the rear titanium skin. In comparison, for the ‘FML-D’ specimen shown in Fig. 6(b), the indented area was larger on its front

FML skin while the failure mode of its rear FML skin was dominated by dishing and cracking. Further, four tearing cracks were observed in the outmost titanium layer of the rear FML skin and the adjacent UHMWPE composite layer was rebounded, resulting in debonding failure. Upon removing both FML skins, localized indentation failure of the

honeycomb core was observed, while the adhesive film remained attached. Nonetheless, in contrast to the case of ‘MF’, lateral compression of honeycomb core was not observed in ‘FML-D’, corresponding to the disappearance of sparks observed from high-speed images.

Fig. 7 presented photographs taken from the side view for the three different types of specimen impacted at selected initial velocities. For all impact velocities considered, the rear FML skins exhibited larger deflection and deformation area, which was responsible for higher energy absorption and lower residual projectile velocity. In addition, skin-core debonding was found in all the ‘MF’ specimens. In sharp contrast, debonding between the FML skin and honeycomb core was not visible, while debonding between the UHMWPE and titanium layers occurred in the FML skins. Fig. 8 presented cross-sectional views of selected sandwich specimens after projectile impact. In the ‘MF’ specimen, more severe debonding between its front skin and honeycomb core was found than either the ‘FML-S’ or ‘FML-D’ specimen. As for the FML skin, either front or rear, delamination between its outmost titanium layer and UHMWPE composite layer was more pronounced.

4.2. Model validation

The developed FE models were quantitatively validated by comparing the calculated residual velocities of the projectile with those experimentally measured, as presented in Table 6: overall, good agreement was achieved for all the three types of sandwich specimen considered. Fig. 9 plotted the numerically simulated deformation and failure modes for selected specimens. While the bulge deformation of FML skins and local deformation of titanium skin were well simulated, the failure modes of all skin types were also well captured. Further, the morphology of honeycomb core was reproduced well relative to that observed experimentally (e.g., the inserts of Fig. 9 for the ‘MF’ specimen). In summary, the validity of FE models developed in this study was established.

4.3. Mechanisms underlying projectile penetration

In the following section, the validated FE models were employed to explore in more detail the physical mechanisms underlying projectile penetration. Fig. 10 compared the simulated penetration processes of ‘MF’ and ‘FML-D’ specimens, both impacted at 500 m/s. For the ‘MF’, its front titanium skin was perforated within the first 10 microseconds. The projectile reached the rear titanium skin before 60 μs, resulting in a faint bulging deformation, followed by shear plugging (as seen in 80 μs). As for the ‘FML-D’, complete penetration of its front FML skin was considerably delayed to 20 μs, so the interaction of the front skin with honeycomb core was stronger, resulting in a larger indentation area. At 60 μs, the projectile just reached the rear skin, causing it to deform till perforation at 110 μs. It was worth noting that the rupture of titanium layer occurred at 80 μs, while the UHMWPE composite layers remained intact. In this case, due to the pushing of the adjacent UHMWPE layer, the deformation area of the titanium layer continued to increase, until

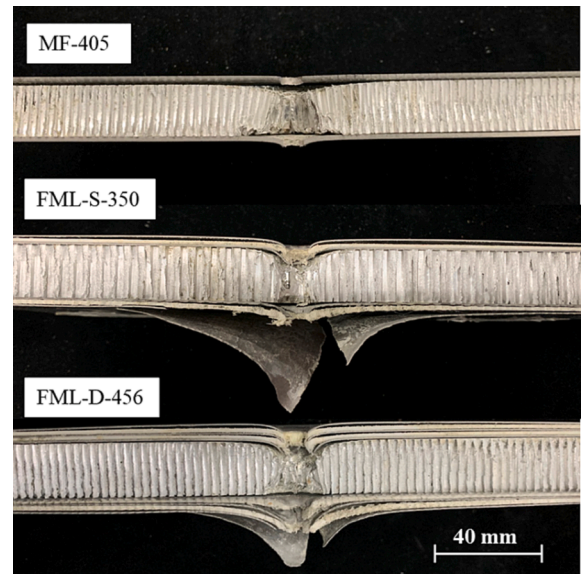


Fig. 8. Cross-sectional views of three different sandwich specimens after projectile penetration at similar impact velocities.

Table 6

Residual velocities of projectile: comparison between experiment and FE simulation.

| Specimen type | Number | Impact velocity (m/s) | Residual velocity (m/s) | | Error (%) |
|---------------|--------|-----------------------|-------------------------|----------------|-----------|
| | | | Experiments | FE simulations | |
| MF | 1 | 405 | 256 | 257 | 0.36 |
| | 2 | 500 | 368 | 353 | 4.08 |
| | 3 | 611 | 476 | 468 | 1.68 |
| FML-S | 1 | 350 | 250 | 216 | 13.60 |
| | 2 | 468 | 384 | 363 | 5.47 |
| | 3 | 622 | 544 | 522 | 4.04 |
| FML-D | 1 | 456 | 267 | 225 | 15.73 |
| | 2 | 550 | 389 | 382 | 1.80 |

the UHMWPE layer was penetrated; Fig. 10(b).

For the three specimen types considered, Fig. 11 compared the numerically calculated energy absorption of individual constituents in each sandwich type, with the initial impact velocity fixed at 500 m/s. For the ‘MF’ specimen, the energy was mainly absorbed by deformation of the front titanium skin, the rear titanium skin and the projectile, while the honeycomb core contributed little to penetration resistance. For the ‘FML-S’, while the UHMWPE layer exhibited excellent energy absorption capability, the FML skin was not hard enough to deform the projectile for the relatively soft UHMWPE layer reduced the stiffness of the FML skin in comparison with its monolithic counterpart. Thus, the energy absorbed via plastic deformation of the projectile was considerably

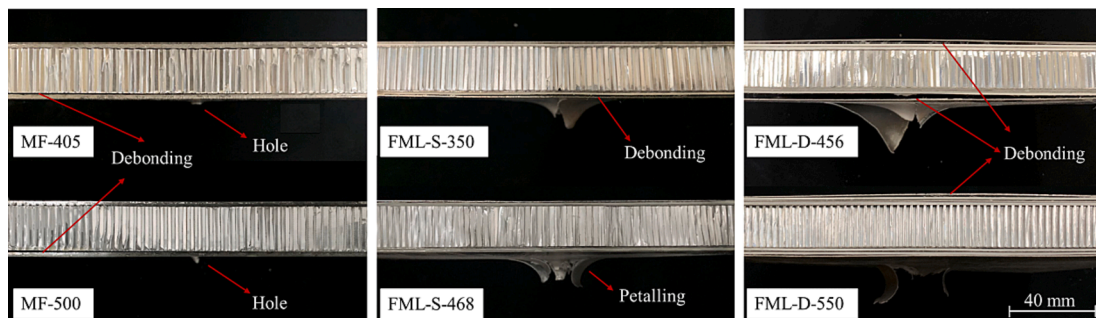


Fig. 7. Side views of three different sandwich specimens after projectile penetration at varying initial impact velocities.

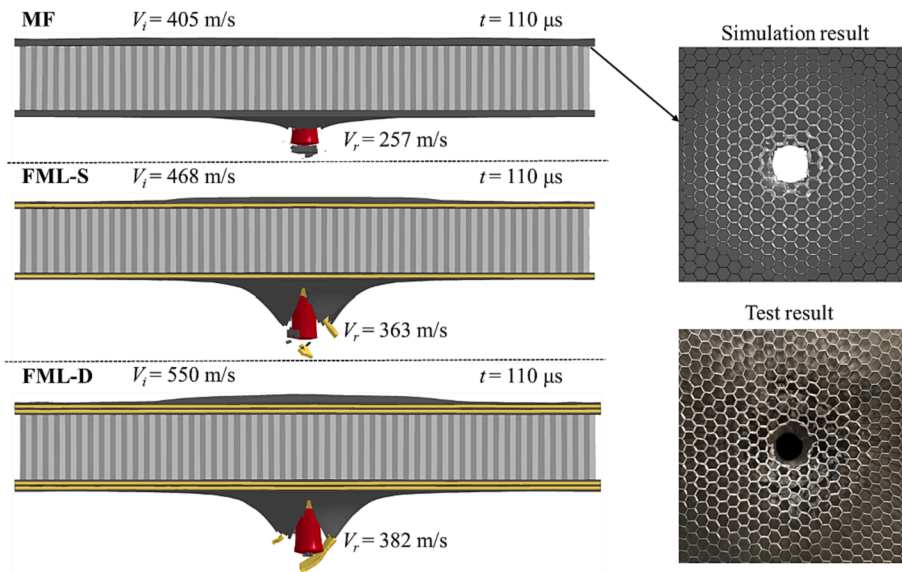


Fig. 9. Numerically simulated deformation and failure modes for three different types of sandwich specimen.

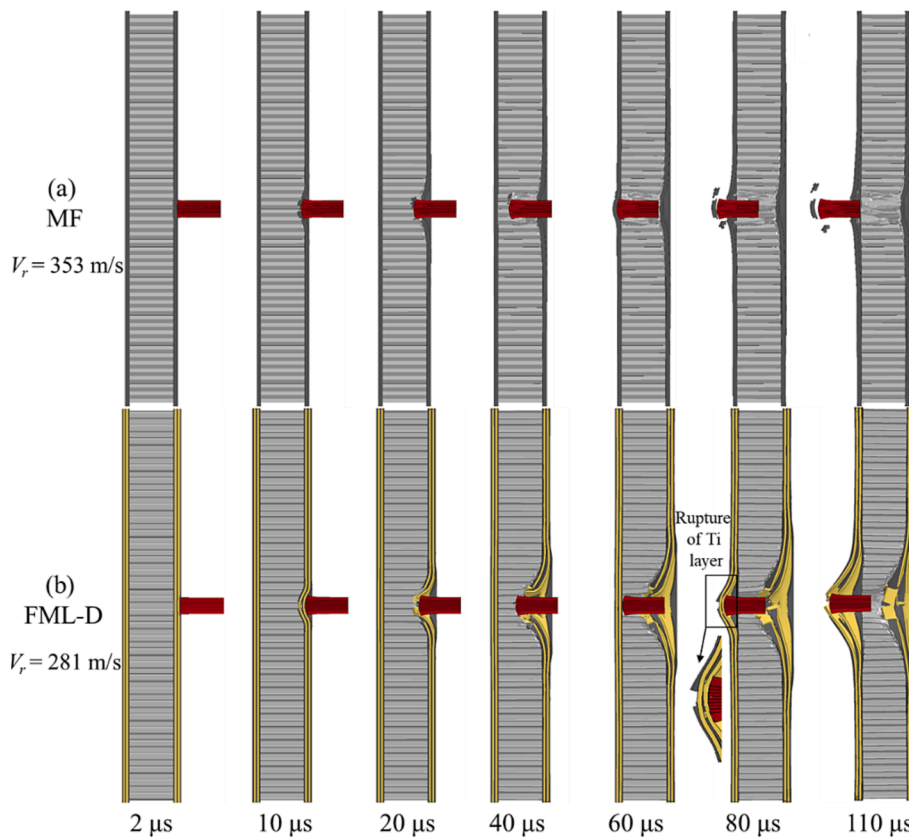


Fig. 10. Numerically simulated penetration processes of (a) 'MF' and (b) 'FML-D' sandwiches impacted at 500 m/s.

reduced, from 126 J to 67.7 J, leading to inferior performance of the 'FML-S'. As for the 'FML-D', although the mass of titanium layers was only three-quarters of that used in the 'MF', the energy absorption of the rear titanium sheets was increased by 24 % due mainly to the transition of deformation modes. As the thickness of a FML skin was increased, the energy dissipated by plastic deformation of the projectile also increased. Meanwhile, the mass proportion of UHMWPE layers in 'FML-D' was 19.3 %, but the corresponding energy absorption proportion was 21.7 %. Thus, the superior penetration resistance of 'FML-D' could be

attributed to the enhanced energy absorption efficiency of titanium layers and incorporation of the UHMWPE composite layers.

4.4. Parametric analysis

In this section, based upon FE simulations, how the number of layers in a FML skin, the thickness distribution of thin titanium layers, and the bonding condition of FML skins would affect the residual velocity of projectile were quantified. The various types of FML skin discussed had

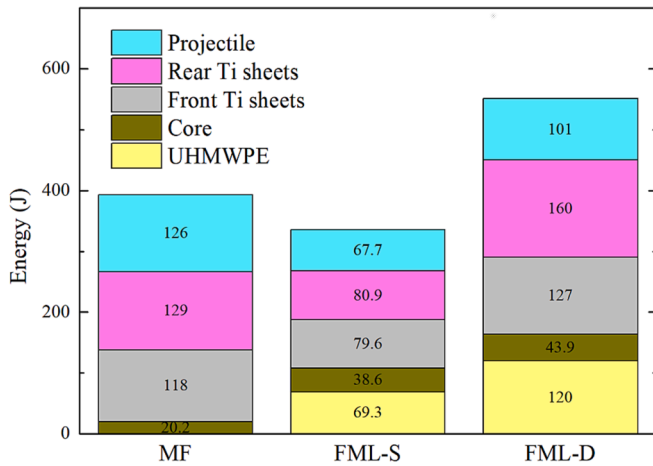


Fig. 11. Energy absorption of different components at an impact velocity of 500 m/s.

the same total thickness and areal density as the ‘FML-D’, as illustrated in Table 7. Notably, to maintain the same areal density, the thickness of ‘FML-S’ skin shown in Table 7 was different from that used in the impact experiments.

4.4.1. Number of layers in FML skin

First, the dependence of residual velocity on the number of layers in a FML skin was investigated, with the initial impact velocity fixed at 500 m/s. Specimen ‘FML-T’ or ‘FML-Q’ indicated that its FML skins consisted of three or four UHMWPE composite layers (Table 7), respectively. As shown in Fig. 12(a), the residual velocity dropped significantly as the number of layers was increased, but the slope gradually decreased. Selected failure modes indicated that the larger out-of-plane deformation of a FML skin with more layers contributed to enhance the ballistic performance of the sandwich. This result was consistent with previous investigations wherein the penetration resistance of UHMWPE laminates was found to be improved as the number of UHMWPE lamina was increased [44,47].

4.4.2. Thickness distribution of titanium layers in FML skin

Fig. 12(b) presented the effect of stacking sequence of titanium layers in a FML skin on residual velocity of projectile. With the initial impact velocity fixed at 500 m/s, five sandwich specimens with different thickness distributions of front and rear titanium layers were investigated, as shown in Table 7. For convenience, let the number symbol ‘I-II’ refer to thickness fractions of front and rear titanium layers, e.g., ‘0-1’ denoted 2 mm UHMWPE/1.5 mm titanium, and ‘1/3-2/3’ denoted 0.5 mm titanium/2 mm UHMWPE/1 mm titanium; Table 7. As illustrated in

Table 7 Illustration of different FML configurations considered in parametric study.

| | FML type | Configuration of the skin |
|---|-----------|---------------------------|
| Number of layers | FML-S | |
| | FML-D | |
| | FML-T | |
| | FML-Q | |
| | | |
| Thickness distribution of titanium layers | ‘0-1’ | |
| | ‘1/3-2/3’ | |
| | ‘1/2-1/2’ | |
| | ‘2/3-1/3’ | |
| | ‘1-0’ | |

Fig. 12(b), the residual velocity varied significantly as the configuration of FML skin was altered. Corresponding failure modes (only those of ‘0-1’ and ‘1-0’ displayed in Fig. 12(b) for brevity) demonstrated that, for either the front or rear FML skin, its front titanium layer was perforated with slightly local deformation, while its rear titanium layer could absorb more energy via larger out-of-plane deformation. However, the deformation of UHMWPE composite layer in the FML skin was restricted by the titanium layer placed behind it, thus weakening its energy absorption efficiency. These competing mechanisms led to the non-monotonic variation trend of residual velocity shown in Fig. 12(b). For the ‘0-1’ configuration, the energy was mainly absorbed by the titanium layer and the UHMWPE composite layer, and the penetration resistance was the highest among the 5 configurations considered. For the ‘2/3-1/3’ configuration, although the energy absorbed by the UHMWPE layer was increased, the energy absorption of titanium layer was greatly decreased, resulting in the worst performance.

4.4.3. Bonding condition

The effect of bonding conditions on residual velocity was also explored numerically. To this end, the configuration ‘1/2-1/2’ (i.e., stacking order of FML skin was 0.75 mm titanium/2 mm UHMWPE/0.75 mm titanium) was selected, with three different types of bonding condition investigated, as shown in Fig. 13. The condition of ‘actual bonding’ corresponded to the case of interface normal strength 41 MPa and an interface shear strength 30 MPa, as described in Section 3.1. Unexpectedly, the residual velocity of the projectile after perforating the sandwich specimen was not sensitive to the bonding conditions considered. This result implied that, when the initial impact velocity exceeded the ballistic limit, the energy dissipated via interface delamination of the FML skins played a minor role in total energy absorption. However, for practical applications, well-bonded FML skins are required for the multifunctional sandwich construction to achieve simultaneous load-bearing and blast/ballistic resistance.

4.5. Multifunctional properties

Traditionally, cellular sandwich plates are envisioned as lightweight load-bearing structures for a wide range of military and civil applications. However, during service, in addition to carry structural loads, these sandwich plates are often subjected to combined blast and fragments loading caused by, say, cased explosives. It is thus of importance to investigate the multifunctional properties of ultralight cellular sandwich plates with UHMWPE FML skins. The results presented in previous sections have demonstrated that the ballistic performance of all-metallic cellular sandwich plates could be enhanced by using UHMWPE FML skins. In this section, to check how the UHMWPE FML skins would affect the other attributes of the proposed sandwich construction, the three-point bending performance and the blast resistance of ‘FML-D’ specimens were evaluated numerically. For illustration, sandwich beams with length 160 mm and width 40 mm were modeled. For comparison, corresponding ‘MF’ specimens were also numerically simulated.

The sandwich beam subjected to three-point bending was simply supported, with a span distance of 100 mm between the two supports. Both the indenter and supports had a diameter of 8 mm, and were treated as rigid bodies. A constant loading speed of 0.08 m/s was applied to the indenter, which had been shown to be sufficiently accurate and computationally efficient for the simulation of quasi-static loading [48].

Fig. 14(a) compared the force versus displacement curves of ‘FML-D’ and ‘MF’ specimens. Replacing the titanium skins with the UHMWPE FML skins altered considerably the bending response of the sandwich beam, elevating significantly its load-bearing capacity. For both the ‘FML-D’ and ‘MF’ specimens, after the initial linear elastic stage, nonlinear increase in force was initiated by local compressive yielding of honeycomb core under the indenter: as shown in Fig. 15(a), plastic buckling and progressive folding of honeycomb core was found near the indenter, and additional plastic buckling could also be observed near the

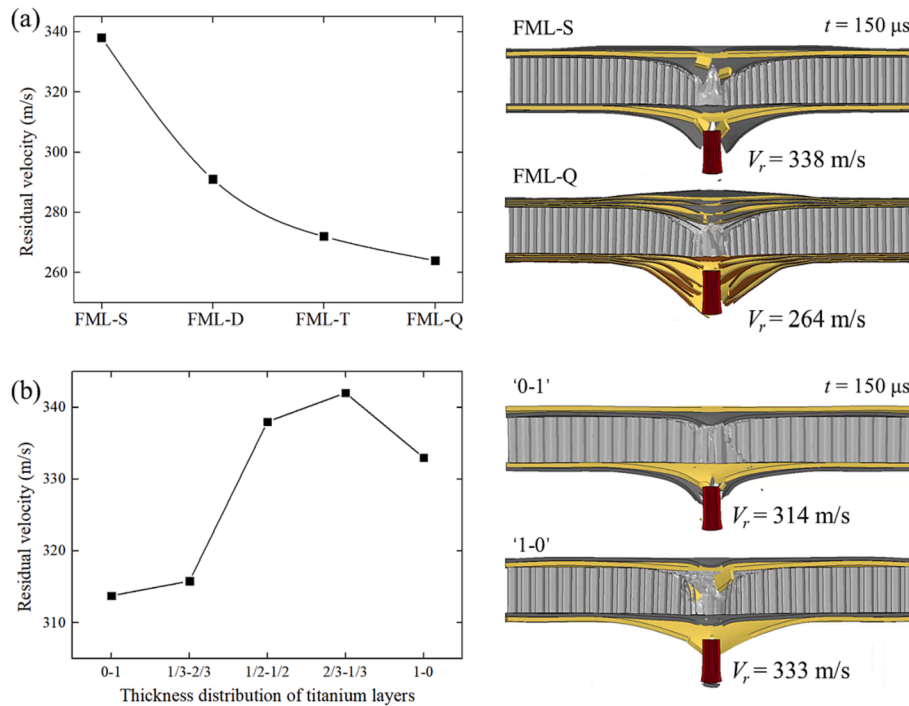


Fig. 12. Numerically calculated dependence of residual velocity on (a) number of layers and (b) thickness distribution of titanium layers in FML skin, with initial impact velocity fixed at 500 m/s.

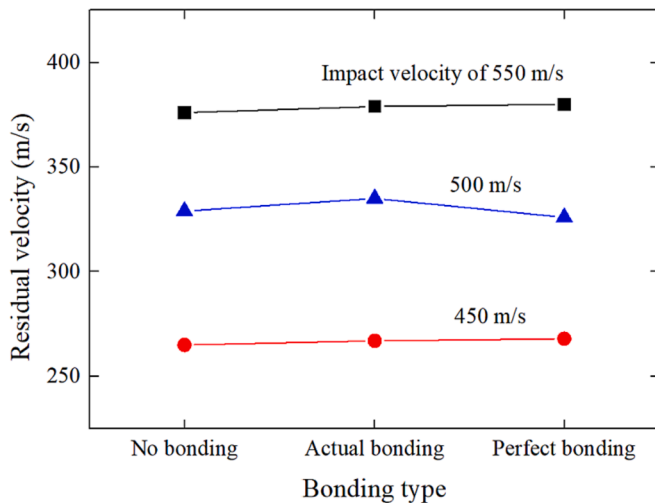


Fig. 13. Influence of bonding condition on residual velocity at selected impact velocities for FML configuration '1/2-1/2'.

two supports. However, a premature failure of 'FML-D' happened at a peak load of 6459 N, corresponding to a displacement of 1.25 mm, which was attributed to the debonding between titanium and UHMWPE layers. Thus, additional simulation was conducted to characterize the bending performance of 'FML-D' with perfect bonded UHMWPE FML skins. As shown in Fig. 14(a), with perfect bonding, premature failure was eliminated in the 'FML-D' sandwich and the peak force could be increased by 57.3 % compared to its 'MF' counterpart.

It has been well established, both experimentally and numerically, that the blast loading on a target could be simulated by the impacting of aluminum foam projectile [49,50]. This technique was employed here to numerically assess the dynamic responses of sandwiches at laboratory scale. Specifically, the sandwich beam subjected to foam impact was end-clamped, with the corresponding nodes fixed in the FE model.

Cylindrical closed-cell aluminum foam with a diameter of 40 mm and a length of 80 mm was used. The aluminum foam had a density of 378.3 kg/m³ and a plateau stress of 4.1 MPa. With the stress versus strain curve of aluminum foam taken from our previous study [50], the *MAT_CRUSHABLE_FOAM constitutive model in LS-DYNA was adopted. The impact velocity of foam projectile was set as 200 m/s, yielding an initial impact impulse of 6 kPa·s.

Fig. 14(b) plotted the mid-span deflection as a function of time for 'MF', 'FML-D' and perfect bonded 'FML-D' specimens. Irrespective of sandwich types, the curve increased monotonously to the maximum deflection, followed by an elastic spring back. Although debonding of the 'FML-D' specimen was activated during deformation, as shown in Fig. 15(b), its maximum deflection was 7.3 mm, which was slightly smaller than that (8.1 mm) achieved by the 'MF' specimen. As for the deformation modes, core compression near the mid-span and core shear near the clamped ends could be observed. Meanwhile, the front part of honeycomb core suffered plastic buckling and progressive folding. The perfectly bonded 'FML-D' performed worse than the 'FML-D' specimen, which could be attributed to boundary failure of the front skin of the former. Nonetheless, the proposed sandwich plate with UHMWPE FML skins was superior to its all-metallic counterpart, due likely to its higher bending resistance shown in Fig. 14(a). It was thus confirmed that replacing the titanium skins of an all-metallic cellular sandwich plate with UHMWPE FML skins not only enhances significantly its ballistic resistance, but also improves its load-bearing capability and blast resistance at the same areal density.

5. Concluding remarks

The main objective of this investigation was to enhance the ballistic performance of ultralight multifunctional cellular sandwich structures without compromising their load-bearing capability and other attributes like energy absorption under impact and blast loadings. Honeycomb sandwich plates with UHMWPE FML skins were proposed, and the effectiveness of using such novel skins to enhance the penetration resistance of sandwich was experimentally explored. Finite element models were validated by comparison with the experimental data, and

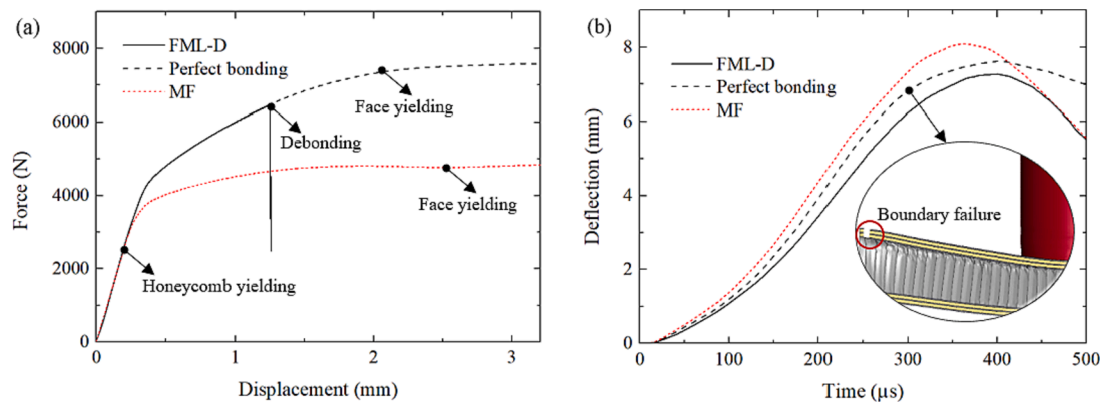


Fig. 14. Comparison between 'FML-D' and 'MF' specimens: (a) force versus displacement curve under quasi-static three-point bending and (b) dynamic response under simulated blast loading.

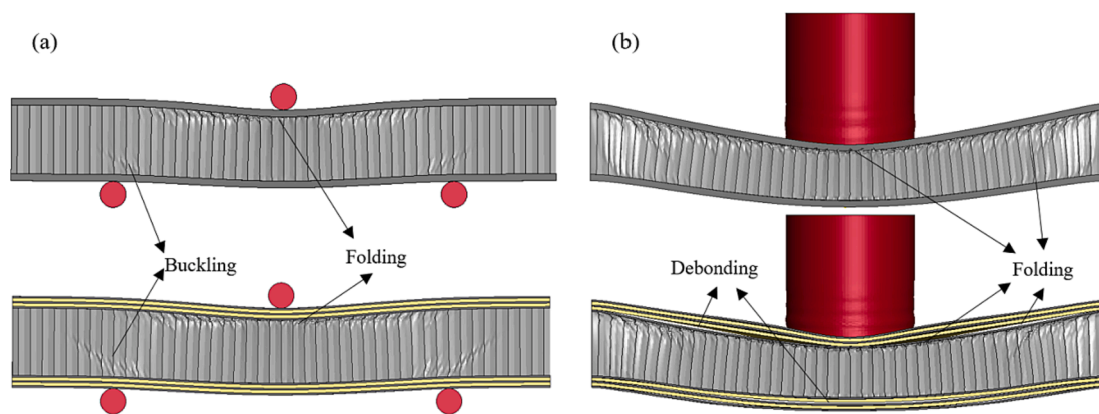


Fig. 15. Deformation and failure modes of 'MF' and 'FML-D' specimens under (a) quasi-static three-point bending and (b) simulated blast loading.

used to investigate the underlying mechanisms and the influence of structural configurations. In addition, the performance under three-point bending as well as impulsive shock loading was also assessed for multifunctional applications. Based on the results, four main conclusions were obtained:

- (1) Replacing the titanium skins with UHMWPE FML skins improved significantly the specific energy absorption with the increase exceeding 23 %, in contrast to the all-metallic honeycomb sandwich having the same areal density. However, no enhancement occurred when maintaining the same thickness (by saving 34 % weight), as the ability of skins to deform the projectile was reduced.
- (2) The complete perforation time of the sandwich with UHMWPE FML skins was considerably delayed by tens of microseconds. For the titanium skins, perforation was accompanied by shear-plugging with weak local deformation, while the FML skins suffered from considerably larger out-of-plane bending deflection and failed by cracking and petaling. Moreover, the deformation region of honeycomb core for sandwiches with FML skins was much larger than that for sandwich with single titanium skins, thus dissipating more impact energy of the projectile.
- (3) The kinetic energy of projectile was mainly absorbed by deformation of the projectile and skins. For FML skins, the metal layers failed before the composite layers. However, interaction between adjacent layers enhanced the energy absorption efficiency of metal layers, due mainly to changes in deformation modes of the skins.

- (4) Increasing the number of layers in a UHMWPE FML skin reduced significantly the residual velocity of projectile. In addition, ballistic response was affected by the thickness distribution of titanium layers, but insensitive to the bonding condition between titanium and UHMWPE layers.
- (5) The UHMWPE FML skins altered the bending response of the sandwich, resulting in enhanced load-bearing capacity. Despite premature failure of UHMWPE FML skins due to the debonding, an increase of 30 % in peak load could be achieved under quasi-static three-point bending. Simultaneously, the shock resistance of the proposed sandwich to impulse loading was slightly improved.

The proposed ultralight cellular sandwich plates with UHMWPE FML skins are promising for weight sensitive applications requiring simultaneous load-bearing capability, ballistic/blast resistance, and additional attributes such as sound absorption and active cooling.

CRediT authorship contribution statement

Rui Zhang: Conceptualization, Methodology, Investigation, Data curation, Writing – original draft. **Bin Han:** Supervision, Conceptualization, Funding acquisition, Project administration, Writing - review & editing. **Yi Zhou:** Software. **Lu-Sheng Qiang:** Visualization. **Qi Zhang:** Project administration. **Qian-Cheng Zhang:** Resources. **Tian Jian Lu:** Writing – review & editing, Supervision, Project administration, Funding acquisition.

Declaration of Competing Interest

The authors declare that they have no known competing financial interests or personal relationships that could have appeared to influence the work reported in this paper.

Data availability

Data will be made available on request.

Acknowledgments

The authors gratefully acknowledge the financial supports by the National Natural Science Foundation of China (11802221, 11972185, 12032010, and 51875441), the Opening Project of MIIT Key Laboratory for Multifunctional Lightweight Materials and Structures, the Fundamental Research Funds for the Central Universities (No. zrzdz2017027), and Key Research and Development Projects of Shaanxi Province (No. 2021GXLH-Z-037).

References

- Schonberg W, Schäfer F, Putzar R. Hypervelocity impact response of honeycomb sandwich panels. *Acta Astronaut* 2010;66(3-4):455–66.
- Caserta GD, Iannucci L, Galvanetto U. Shock absorption performance of a motorbike helmet with honeycomb reinforced liner. *Compos Struct* 2011;93(11):2748–59.
- Wang W, Yang X, Han B, Zhang Q, Wang X, Lu T. Analytical design of effective thermal conductivity for fluid-saturated prismatic cellular metal honeycombs. *Theor Appl Mech Lett* 2016;6(2):69–75.
- Balcı O, Çoban O, Bora MÖ, Akagündüz E, Yağcı EB. Experimental investigation of single and repeated impacts for repaired honeycomb sandwich structures. *Mater Sci Eng A* 2017;682:23–30.
- Yang M, Han B, Su PB, Wei ZH, Zhang Q, Zhang QC, et al. Free vibration and axial compression of all-metallic cylindrical and truncated conical sandwich shells with corrugated cores. *J Sandwich Struct Mater* 2021;23(6):2274–95.
- Quan C, Han B, Hou Z, Zhang Q, Tian X, Lu TJ. 3d printed continuous fiber reinforced composite auxetic honeycomb structures. *Compos B Eng* 2020;187:107858.
- Hutchinson JW, Xue Z. Metal sandwich plates optimized for pressure impulses. *Int J Mech Sci* 2005;47(4-5):545–69.
- Wang X, Yu RP, Zhang QC, Li L, Li X, Zhao ZY, et al. Dynamic response of clamped sandwich beams with fluid-filled corrugated cores. *Int J Impact Eng* 2020;139:103533.
- Han B, Zhang ZJ, Zhang QC, Zhang Q, Lu TJ, Lu B-H. Recent advances in hybrid lattice-cored sandwiches for enhanced multifunctional performance. *Extreme Mech Lett* 2017;10:58–69.
- Sun S, Sheng Y, Feng S, Jian Lu T. Heat transfer efficiency of hierarchical corrugated sandwich panels. *Compos Struct* 2021;272:114195.
- Yan H, Zhang Q, Chen W, Xie G, Dang J, Lu TJ. An X-lattice cored rectangular honeycomb with enhanced convective heat transfer performance. *Appl Therm Eng* 2020;166:114687.
- Yan H, Yang X, Lu T, Xie G. Convective heat transfer in a lightweight multifunctional sandwich panel with X-type metallic lattice core. *Appl Therm Eng* 2017;127:1293–304.
- Tang Y, Li F, Xin F, Lu TJ. Heterogeneously perforated honeycomb-corrugation hybrid sandwich panel as sound absorber. *Mater Des* 2017;134:502–12.
- Tang Y, Xin F, Lu TJ. Sound absorption of micro-perforated sandwich panel with honeycomb-corrugation hybrid core at high temperatures. *Compos Struct* 2019;226:111285.
- Yungwirth CJ, Wadley HNG, O'Connor JH, Zakraysek AJ, Deshpande VS. Impact response of sandwich plates with a pyramidal lattice core. *Int J Impact Eng* 2008;35(8):920–36.
- Wadley HNG, Dharmasena KP, O'Masta MR, Wetzel JJ. Impact response of aluminum corrugated core sandwich panels. *Int J Impact Eng* 2013;62:114–28.
- Xie WH, Meng SH, Ding L, Jin H, Du SY, Han GK, et al. High-temperature high-velocity impact on honeycomb sandwich panels. *Compos B Eng* 2018;138:1–11.
- Zhang QN, Zhang XW, Lu GX, Ruan D. Ballistic impact behaviors of aluminum alloy sandwich panels with honeycomb cores: An experimental study. *J Sandwich Struct Mater* 2018;20(7):861–84.
- Sun G, Chen D, Wang H, Hazeli PJ, Li Q. High-velocity impact behaviour of aluminium honeycomb sandwich panels with different structural configurations. *Int J Impact Eng* 2018;122:119–36.
- Wadley HNG, O'Masta MR, Dharmasena KP, Compton BG, Gamble EA, Zok FW. Effect of core topology on projectile penetration in hybrid aluminum/alumina sandwich structures. *Int J Impact Eng* 2013;62:99–113.
- Zhang R, Han B, Lu TJ. Confinement effects on compressive and ballistic performance of ceramics: a review. *Int Mater Rev* 2021;66(5):287–312.
- Ni CY, Hou R, Xia HY, Zhang QC, Wang WB, Cheng ZH, et al. Perforation resistance of corrugated metallic sandwich plates filled with reactive powder concrete: experiment and simulation. *Compos Struct* 2015;127:426–35.
- Yungwirth CJ, Radford DD, Aronson M, Wadley HNG. Experiment assessment of the ballistic response of composite pyramidal lattice truss structures. *Compos B Eng* 2008;39(3):556–69.
- Sinmazçelik T, Avcu E, Bora MÖ, Çoban O. A review: Fibre metal laminates, background, bonding types and applied test methods. *Mater Des* 2011;32(7):3671–85.
- Ramadhan AA, Abu Talib AR, Mohd Rafie AS, Zahari R. High velocity impact response of Kevlar-29/epoxy and 6061-T6 aluminum laminated panels. *Mater Des* 2013;43:307–21.
- Hoo Fatt MS, Lin C, Reilock DM, Hopkins DA. Ballistic impact of GLARE™ fiber-metal laminates. *Compos Struct* 2003;61(1-2):73–88.
- Seyed Yaghoubi A, Liaw B. Thickness influence on ballistic impact behaviors of GLARE 5 fiber-metal laminated beams: experimental and numerical studies. *Compos Struct* 2012;94(8):2585–98.
- Xu MM, Huang GY, Dong YX, Feng SS. An experimental investigation into the high velocity penetration resistance of CFRP and CFRP/aluminium laminates. *Compos Struct* 2018;188:450–60.
- He W, Wang L, Liu H, Wang C, Yao Lu, Li Q, et al. On impact behavior of fiber metal laminate (FML) structures: a state-of-the-art review. *Thin-Walled Struct* 2021;167:108026.
- Liu C, Zhang YX, Li J. Impact responses of sandwich panels with fiber metal laminate skins and aluminium foam core. *Compos Struct* 2017;182:183–90.
- Ghalami-Chooabar M, Sadighi M. Investigation of high velocity impact of cylindrical projectile on sandwich panels with fiber-metal laminates skins and polyurethane core. *Aerosp Sci Technol* 2014;32(1):142–52.
- Reyes Villanueva G, Cantwell WJ. The high velocity impact response of composite and FML-reinforced sandwich structures. *Compos Sci Technol* 2004;64(1):35–54.
- Karthikeyan K, Russell BP, Fleck NA, Wadley HNG, Deshpande VS. The effect of shear strength on the ballistic response of laminated composite plates. *Eur J Mech A Solids* 2013;42:35–53.
- Nguyen LH, Ryan S, Cimpoeu SJ, Mouritz AP, Orifici AC. The efficiency of ultra-high molecular weight polyethylene composite against fragment impact. *Exp Mech* 2016;56(4):595–605.
- Zhang R, Qiang LS, Han B, Zhao ZY, Zhang QC, Ni CY, et al. Ballistic performance of UHMWPE laminated plates and UHMWPE encapsulated aluminum structures: numerical simulation. *Compos Struct* 2020;252:112686.
- Zhao ZN, Han B, Zhang R, Zhang Qi, Zhang QC, Ni CY, et al. Enhancement of UHMWPE encapsulation on the ballistic performance of bi-layer mosaic armors. *Compos B Eng* 2021;221:109023.
- Li X, Zhang X, Guo Y, Shim VPW, Yang J, Chai GB. Influence of fiber type on the impact response of titanium-based fiber-metal laminates. *Int J Impact Eng* 2018;114:32–42.
- Rafiee R, Yazdanparast R, Ghorbanhosseini A. Bending analysis of molded composite grating panels: theoretical and experimental investigations. *Fibers Polym* 2021;22(6):1653–63.
- Yazdanparast R, Rafiee R. Developing a homogenization approach for estimation of in-plan effective elastic moduli of hexagonal honeycombs. *Eng Anal Boundary Elem* 2020;117:202–11.
- Hallquist JO. LS-DYNA keyword user's manual version 971. Livermore Software Technology Corporation; 2007.
- Technical Data Sheet LOCTITE® EA E-120HP. Henkel Corporation; 2020.
- Johnson GR, Cook WH. Fracture characteristics of three metals subjected to various strains, strain rates, temperatures and pressures. *Eng Fract Mech* 1985;21(1):31–48.
- Serjoui A, Gour G, Zhang X, Idapalapati S, Tan GEB. On improving ballistic limit of bi-layer ceramic-metal armor. *Int J Impact Eng* 2017;105:54–67.
- Zhang R, Han B, Zhong JY, Qiang LS, Ni CY, Zhang Q, et al. Enhanced ballistic resistance of multilayered cross-ply UHMWPE laminated plates. *Int J Impact Eng* 2022;159:104035.
- Lässig T, Nguyen L, May M, Riedel W, Heisserer U, van der Werff H, et al. A non-linear orthotropic hydrocode model for ultra-high molecular weight polyethylene in impact simulations. *Int J Impact Eng* 2015;75:110–22.
- Menna C, Asprone D, Caprino G, Lopresto V, Prota A. Numerical simulation of impact tests on GFRP composite laminates. *Int J Impact Eng* 2011;38(8-9):677–85.
- Haris A, Tan VBC. Effects of spacing and ply blocking on the ballistic resistance of UHMWPE laminates. *Int J Impact Eng* 2021;151:103824.
- Wang Z, Li Z, Xiong W. Numerical study on three-point bending behavior of honeycomb sandwich with ceramic tile. *Compos B Eng* 2019;167:63–70.
- Radford DD, Deshpande VS, Fleck NA. The use of metal foam projectiles to simulate shock loading on a structure. *Int J Impact Eng* 2005;31(9):1152–71.
- Yu RP, Wang X, Zhang QC, Li L, He SY, Han B, et al. Effects of sand filling on the dynamic response of corrugated core sandwich beams under foam projectile impact. *Compos B Eng* 2020;197:108135.